Orographic and convective gravity waves above the Alps and Andes mountains during GPS radio occultation events – a case study

Rodrigo Hierro[1], Andrea K. Steiner[2], Alejandro de la Torre[1], Peter Alexander[3], Pablo Llamedo[1], Pablo Cremades[4]

Correspondence to: Rodrigo Hierro (rhierro@austral.edu.ar)

[1] Facultad de Ingeniería, Universidad Austral and CONICET, Pilar, Provincia de Buenos Aires B1629ODT, Argentina

[2] Wegener Center for Climate and Global Change (WEGC) and Institute for Geophysics, Astrophysics, and Meteorology/Institute of Physics, University of Graz, Graz, Austria

[3] IFIBA, CONICET, Ciudad Universitaria, Buenos Aires, Argentina

[4] Facultad de Ciencias Exactas y Naturales, Universidad Nacional de Cuyo, Argentina

Abstract. Gravity waves (GW) and convective systems play a fundamental role in atmospheric circulation, weather, and climate. Two usual main sources of GW are orographic effects triggering mountain waves and convective activity. In addition, GW generation by fronts and geostrophic adjustment must be considered too. The utility of Global Positioning System (GPS) radio occultation (RO) observations for the detection of convective systems is tested. A collocation database between RO events and convective systems over sub-tropical to mid-latitude mountain regions, close to the Alps and Andes is built. From the observation of large amplitude GW structures and the absence of jets and fronts, subsets of RO profiles are sampled. A representative case study among those considered at each region is selected and analyzed. The case studies are investigated using mesoscale WRF simulations, ERA Interim reanalyses data and the measured RO T profiles. The absence of fronts or jets during both case studies reveals similar relevant GW features (main parameters, generation and propagation). Orographic and convective activity generates the observed GW. Mountain waves above the Alps reach higher altitudes than close to the Andes. In this last case a critical layer prevents for the propagation of GW packets up to stratospheric heights. The case studies are selected also because they illustrate how the observational window for GW observations through RO profiles admits a misleading interpretation of structures at different altitude ranges. From recent results, the distortion introduced in the measured atmospheric vertical wavelengths by one of the RO events is illustratively discussed. In the analysis, both the elevation angle of the sounding path (line of tangent points) and the gravity wave aspect ratio estimated from the simulations and the line of sight, are taken into account. In both case studies, a considerable distortion, over- and underestimation of the vertical wavelengths measured by RO may be expected.

1. Introduction

The Global Positioning System (GPS) radio occultation (RO) technique has been proven to be a powerful tool to analyze meteorological tropospheric features with a moderate/high spatial and temporal resolution in essentially any meteorological condition. Its ability to penetrate clouds allows to retrieve temperature (T) and water vapor pressure (e), amongst several other atmospheric variables with high vertical resolution close to the near surface. Vertical profiles of T are provided with an accuracy of less than1 K (e.g., Kursinski et al., 1997; Steiner and Kirchengast, 2005; Scherllin-Pirscher et al., 2011; 2017) in the troposphere to lower stratosphere and specific humidity with an accuracy of about 0.3 g kg^{-1} to 0.1 g kg^{-1} in the lower to middle troposphere (Kursinski and Gebhardt, 2014). Although measurements are taken irregularly in time and space, they provide a global coverage. Data are available from several missions such as the CHAllenging Minisatellite Payload (CHAMP), Satélite deAplicaciones Científicas-C (SAC-C), Gravity Recovery and Climate Experiment (GRACE), or the Formosa Satellite mission-3/ Constellation Observing System for Meteorology, Ionosphere, and Climate mission (hereafter referred to as COSMIC), and found to be of high quality and consistency in the troposphere and lower stratosphere (e.g., Steiner et al., 2011; 2013; Angerer et al., 2017, this AMT special issue).

Biondi et al. (2011) recognized double tropopause events using bending angle (BA) anomalies derived from GPS RO measurements from different missions. Later, Biondi et al. (2014) found that the GPS RO technique is useful for understanding the thermal structure of tropical cyclones and possible overshootings into the stratosphere. The complexity of the relationship between deep convection and flow convergence over mountains has been widely studied. Demko et al. (2009) showed that during days with deep convection, the convergence over mountains is weaker than on days when deep convection does not occur.

Over the Alps, considering the kinematic and dynamic features of divergence, flow splitting or mesoscale vortices, it is possible to find regions which initiate or intensify the storms (Bica et al., 2007). Thermally driven flows over the Alps are associated to convergence caused by large-scale topographic heat flow (Langhans et al., 2011). These flows supply moisture from source regions close to the surface, which stimulates the initiation of deep convection (e. g. Barthlott et al., 2006). Gladich et al. (2011) mentioned that southward oriented reliefs receive more solar radiation, resulting in a warmer atmosphere in comparison with flat terrain. Also, the orography presents a negative energetic balance as compared to flat regions.

Extratropical regions in the Southern Hemisphere show strong wave activity close to the Andes and to the Antarctic Peninsula (e.g., Eckermann and Preusse, 1999; de la Torre et al., 2012; Hierro et al., 2013). The eastern side of the Andes at mid-latitudes, between the subtropical and polar jets (Houze, 2012), is a natural laboratory for gravity waves (GW), in particular mountain waves (MW). The dynamic processes involved in convection over this region have been analysed, e.g., by de la Torre et al. (2004), who found that anabatic winds act as triggering mechanism in the presence of moist enthalpy under unstable

conditions. A relationship between MW and the development of deep convection was found by de la
75 Torre et al. (2011). Through the design of several non-dimensional numbers related to storms
development and MW energy, Hierro et al. (2013) found that MW are able to provide the necessary
energy to overcome a surface stable layer. Vertically propagating short-period GW strongly affect the
general circulation as well as the structure of the middle atmosphere (e.g., Dutta et al., 2009).

Convective activity is one of the most important sources of GW through the release of latent heat,
80 contributing to the interaction between waves and mean flow in the middle atmosphere (e.g., Alexander,
1995; Pandya and Alexander, 1999). When a convective cloud reaches the mean flow, waves which
propagate upstream are generated (Beres et al., 2002 and references therein). Convective instability, in
turn, yields oscillatory movements, which give place to GW that propagate vertically as a harmonic
oscillator (e.g., Fritts and Alexander, 2003). Several authors have analyzed the main mechanisms which
85 describe the possible sources of gravity waves generated by convection. In the "obstacle effect", the
background finds a barrier given by the convective flow (Clarke et al., 1986). Fovell et al. (1992),
proposed a mechanism where updrafts and downdrafts reach the tropopause, generating high-frequency
GW. Röttger (1991) studied penetrating cumulus convection which generates GW by transferring kinetic
energy from the troposphere to the lower stratosphere.

90 Evan et al. (2012) determined that the Weather Research and Forecasting (WRF) mesoscale model
(Skamarock et al., 2008) is able to simulate stratospheric GW, when it is run under actual boundary
conditions. It was also possible to resolve GW generated by convection in the tropics. Stephan and
Alexander (2014), in turn, showed that WRF physics parameterizations are not decisive to get good
results from GW simulations. From WRF simulations above the Southern Andes, de la Torre et al. (2012)
95 detected systematic large-amplitude, stationary, nonhydrostatic GW structures, forced by the mountains
up to the lower stratosphere and persisting for several hours. Their dominant modes were characterized by
horizontal wavelengths (λ_H) of around 50 km. The vertical wavelengths (λ_Z) were estimated to be
between 2 km and 11 km. Over the Andes region, de la Torre et al. (2011) detected two main modes of
mountain waves with large amplitude and high intrinsic frequency. Over the same region, Hierro et al.
100 (2013) found stationary modes with λ_H between 40 km and 160 km and λ_Z of around 7 km. de la Torre et
al. (2015), analyzing storms in the presence of MW, distinguished two different structures in vertical
wind simulations. Both of them seem to be fixed to the mountains, defining systematic updraft and
downdraft sectors. GW parameters were analyzed from band-pass and wavelet analysis, indicating for the
cases analyzed the presence of short λ_H and long λ_Z, as expected for high intrinsic period GW.

105 The motivation of the present work is two folded: First, to find a set of collocations among GPS RO *BA*
and *T* profiles and mesoscale sub-tropical convective systems under reasonable conditions of proximity in
space and time occurrence over orographic regions (Alps and Andes). We use this dataset to test the
utility of Global Positioning System (GPS) radio occultation (RO) observations for the detection of
convective systems. To detect the cloud top altitude from the RO profiles, we apply a technique based in
110 the anomay in the *BA*. Secondly, the GW structures are analyzed and discussed for two selected case
studies detected in the absence of jets and fronts, from high resolution mesoscale model simulations and
reanalysis data. The possible determination or misleading interpretation of GW parameters from GPS RO

is discussed in detail for these case studies. Sect. 2 outlines the RO data used and the methodology applied and describes the two subsets of RO events retrieved during convective activity close to Alps and
115 Andes ranges. In Sect. 3, one case study at each region is selected and relevant GW features are analyzed from the simulation, the reanalysis data and the measurement of both RO events. In Sect. 4, conclusions are given.

2. Data and methodology

120 The utility of RO observations for the investigation of convective systems (Biondi et al, 2012; 2015b) and GW over orographic regions in Europe and South America (Alps and Andes mountains) is tested. It is known that a sharp spike in RO *BA* is highly correlated to the top of the cloud, corresponding to anomalously cold temperatures within the cloud. Above the cloud, the temperature returns to background conditions, and a strong inversion appears above the cloud top. For usual tropospheric cloud tops, the *T*
125 lapse rate within the cloud often approaches a moist adiabat, consistent with rapid undiluted ascent within the convective systems.

We built a collocation database between RO observations and mesoscale convective systems over sub-tropical to mid-latitude mountain regions. The selected regions for the Alps and Andes are [40°N to 55°N, 0°E to 20°E] and [20°S to 40°S, 60°W to 74°W], respectively (Fig. 1). We use RO data processed at the
130 Wegener Center for Climate and Global Change (WEGC) with the Occultation Processing System (OPS) version 5.6 (Schwärz et al., 2016), based on excess phase and orbit data version 2010.2640 from the University Corporation for Atmospheric Research (UCAR) from the CHAMP, SAC-C, GRACE, and COSMIC missions. We analyse *BA* and *T* profiles which are available from near surface up to 40 km altitude with 100 m vertical sampling.

135
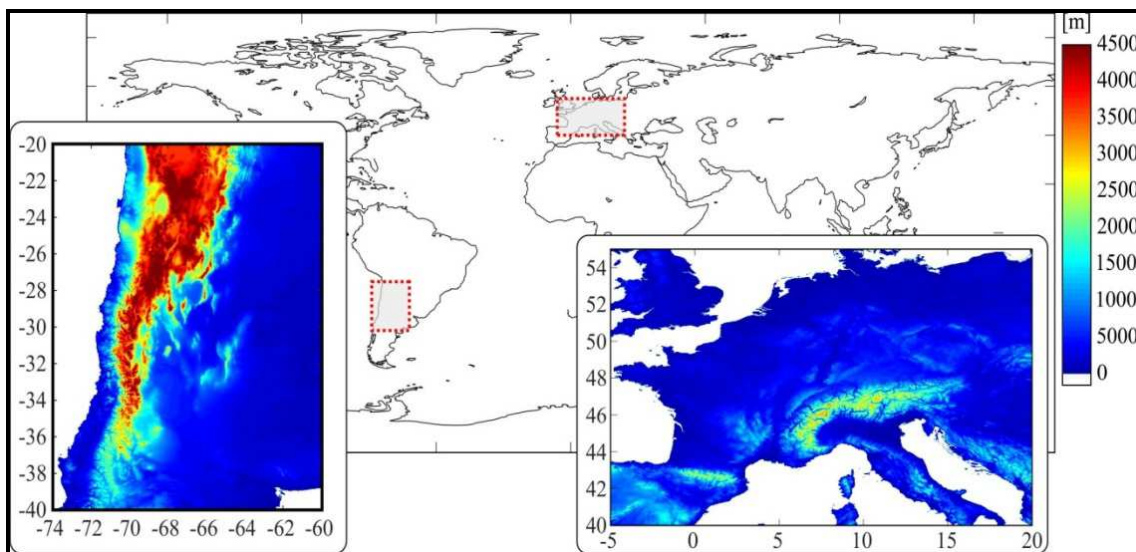
Figure 1: The Alps (right) and Andes (left) regions selected to build a collocation database between RO data and cloud data over sub-tropical to mid-latitude mountain regions. Convective systems are located in time and space using the global deep convective tracking database of the International Satellite Cloud

140   Climatology Project (ISCCP) (Rossow et al., 1996), from January 2006 to July 2008. This period was chosen due to the constraints and limitations imposed by the ISCCP database and the COSMIC data. The first source, available between 1983 and 2008, is currently incomplete and being re-processed. The global ISCCP data set, with a horizontal grid resolution of 30 km and a nominal time resolution of 3 h, is based on brightness temperatures from geostationary satellite measurements. It provides information on

145   the location and extent of mesoscale deep convective cloud systems and their properties. The parameters extracted from ISCCP data, are: time of occurrence, center (mass center) and radius of the storm. The COSMIC mission started in June 2006.

The selection criterion applied in the present work considers the position of the RO observation with respect to the center of the storm, thus providing 294 and 50 collocations at the Alps and Andes regions

150   respectively . According to this criterion, it is observed whether the latitude and longitude corresponding to the mean tangent point (TP) belonging to each RO profile is located within a radius of 100 km with respect to the center of the storm, as provided by ISCCP. A maximum time interval of 3 h was allowed between each RO event and the data from ISCCP. The collocated events were selected using cloud data from geostationary satellites METEOSAT (Europe) and GOES (South America) (Fig. 2).
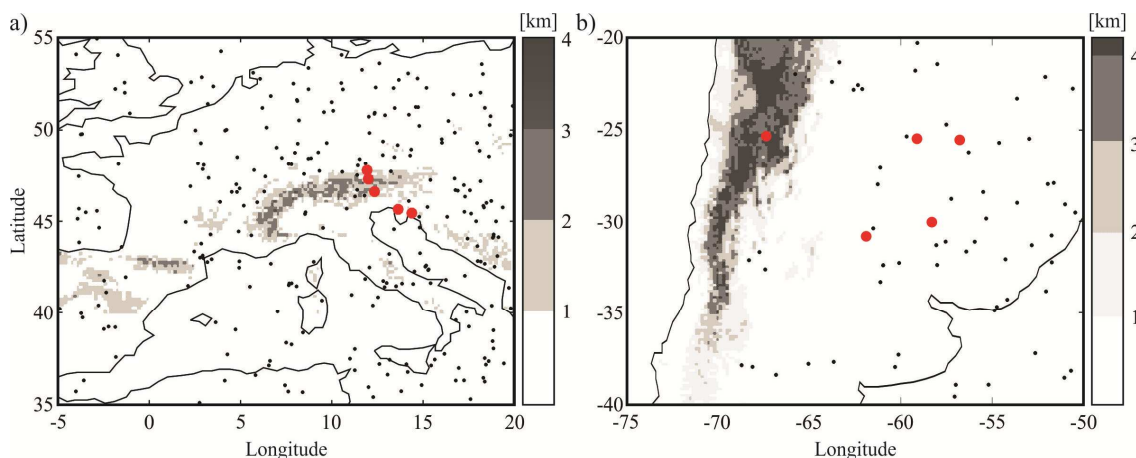
155

Figure 2. Collocated events between GPS RO profiles and convective systems. The latitude and longitude corresponding to the mean tangent point belonging to each RO is located within a radius of 100 km respect to the center of the storm. It is detected in a time interval less than 3 hours. The Alps region (-left- 294 collocations). The Andes region (-right- 50 collocations).

160

The collocated RO *BA* and *T* profiles were further used to determine the vertical structures of sub-tropical convective systems over orographic regions. In order to detect the cloud top altitude with RO, we applied the anomaly technique developed by Biondi et al. (2013) for anomalous atmospheric profile and cloud top detection of convective systems. Each *BA* and *T* profile collocated with a storm was referenced against a

165   RO background reference climatology profile, which was extracted for the same location and the same month from the global RO *BA* and *T* reference climatology, respectively (for details see Biondi et al. (2017)). We then subtracted the collocated RO reference climatology profile from the individual RO profile. *BA* was normalized with respect to the reference climatology profile in order to obtain a fractional

anomaly profile. The cloud top altitude is represented as a pronounced spike in the vertical *BA* anomaly structure and correspondingly, in the *T* anomaly profile.

Taking into account the wave signatures observed in the RO *T* profiles (see below), GW were analyzed from two different data sources: mesoscale model simulations and ERA Interim reanalyses data. The WRF simulations (Skamarock et al., 2008) were performed using 1°×1° National Center of Enviromental Prediction (NCEP) Global Final Analysis (FNL), as boundary conditions. They are conducted in four nested domains (27 km, 9 km, 3 km, and 1 km respectively) with 60 vertical levels. A sponge layer was applied in the upper 3 km. The size of the inner domain in the Alps region is about 300 km x 200 km and that of the Andes region about 300 km x 300 km. For each domain, the microphysical schemes used were the following: WRF Single Moment-6 class (WSM6; Hong et al., 2004); Yonsei University (YSU; Hong et al., 2006) to represent the planetary boundary-layer (PBL) physics; Rapid Radiative Transfer Model Longwave (RRTM; Mlawer et al., 1997) and MM5 Dudhia Shortwave (Dudhia scheme; Dudhia, 1989) for radiation processes; the Noah land surface model (developed jointly by NCAR and NCEP; Skamarock et al., 2008) and Monin–Obukhov scheme; (Monin and Obukhov, 1954) for surface physics and thermal diffusion processes respectively. The cumulus parameterization used was the New Grell scheme (Grell3; (Grell and Devenyi, 2002)) for the first two domains, while no-cumulus parameterization was selected for the two inner one.

In the present study, a GW climatology from the available limited number of collocated cases is not intended. Instead, by focusing on selected large amplitude RO *T* profiles, wave features at both mountain subtropical regions are compared. In doing so, five collocations were pre-selected in each region (central panels in Fig. 3a-b). All of the pre-selected collocations show some spikes in the *BA* profile, from which one is correlated with the cloud top of the corresponding convective structure. Large amplitude oscillations that may be associated to hydrostatic and/or non hydrostatic GW structures are evident. The analysis is further conducted on two peculiar case studies (central frames in Fig. 3a-b), defined by the simultaneous absence of jets and fronts. When these last GW sources (e.g. Fritts and Alexander, 2003) coexist with other sources, the analyses is expectedly more intricated. In the present case studies, GW structures are conceivably limited to orographic and/or convective sources. The RO case studies exhibit attractive oscillatory features and correspond, in the Alps region, to 02 Feb 2008, 17:24 UTC (47.29°N, 12.02°W) and in the Andes region to 19 Dec 2006, 16:56 UTC (25.35°S, 67.37°W).

205
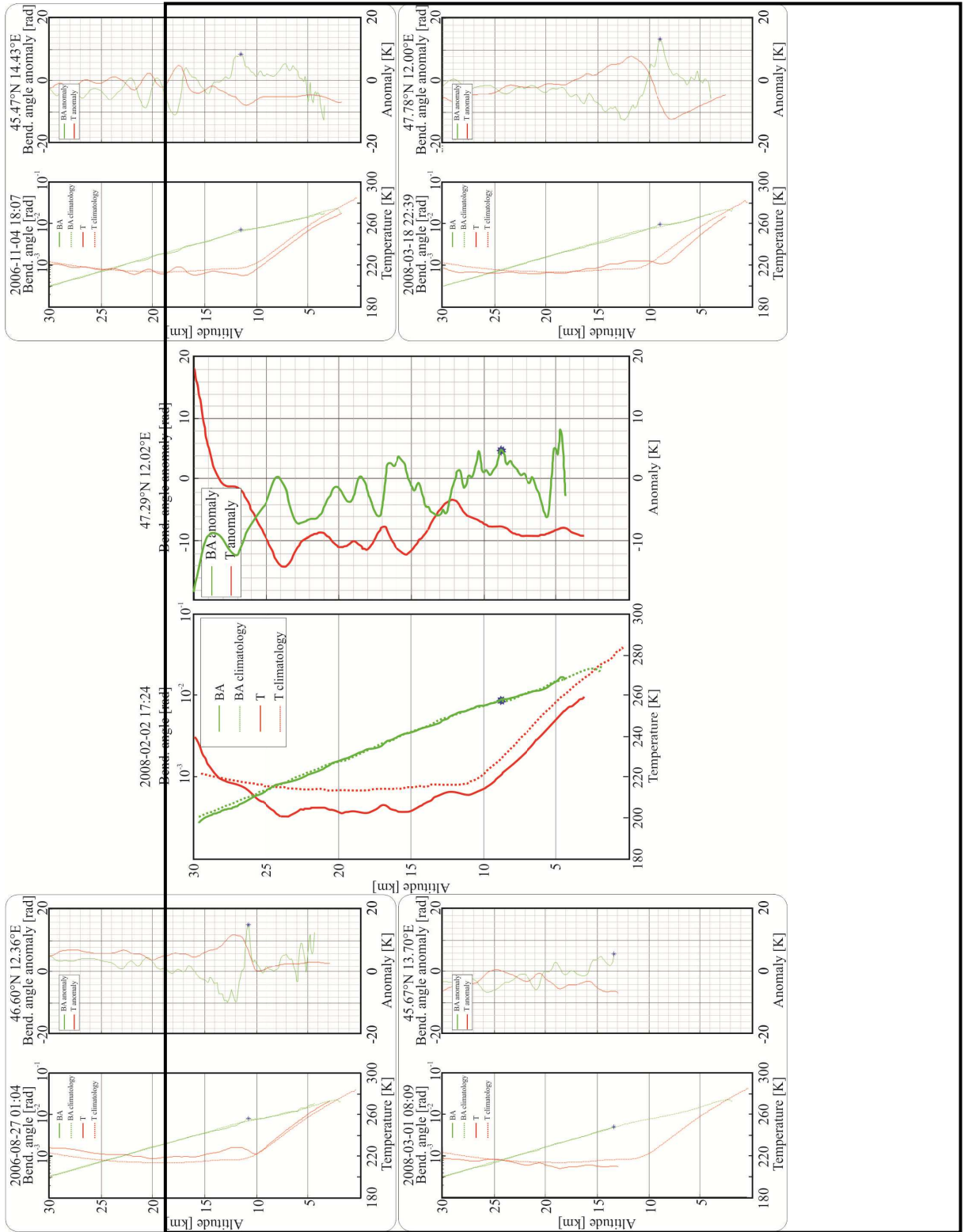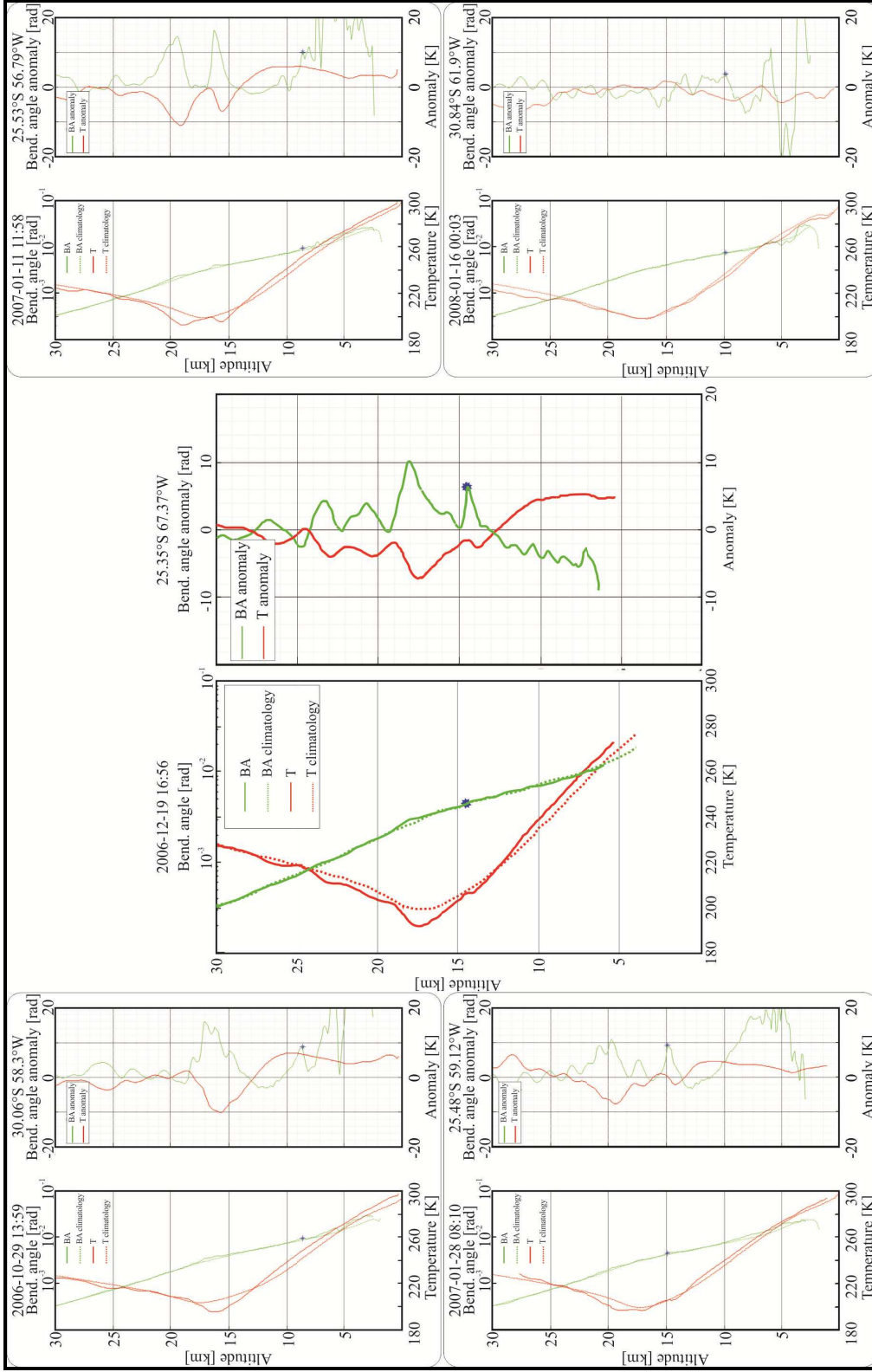
210   Figure 3: Pre-selected collocations between GPS RO profiles and convective developments in a) the Alps region and b) the Andes region . Shown are absolute profiles and anomaly profiles for bending angle (green) and temperature (red) and the respective climatology profile (dotted). The cloud top height is indicated by a blue star. The collocations pre-selected for case studies are based on observed large amplitude wave features in the RO T profiles. The two selected case studies are based on the

215   simultaneous absence of GW sources given by jets and fronts.

3. WRF model simulations, ERA Interim reanalyses data and GPS RO observations

220   The GW in the two selected study cases at the Alps and Andes region are investigated from WRF numerical simulations, ERA Interim reanalyses data and the collocated GPS RO observed profiles.

3.1. Case study at the Alps region

3.1.1. *Numerical simulations of GW structures*

225   At the Alps region, the dynamic and thermodynamic parameters are simulated. In Fig. 4 the vertical air velocity (δw) in the considered area is shown. Two altitude levels (8 km and 12.5 km) are chosen, above and below the cloud tops (situated at 9.8 km height) at 17:00 UTC. The δw field is represented a few minutes before the RO event (17:24 UTC).
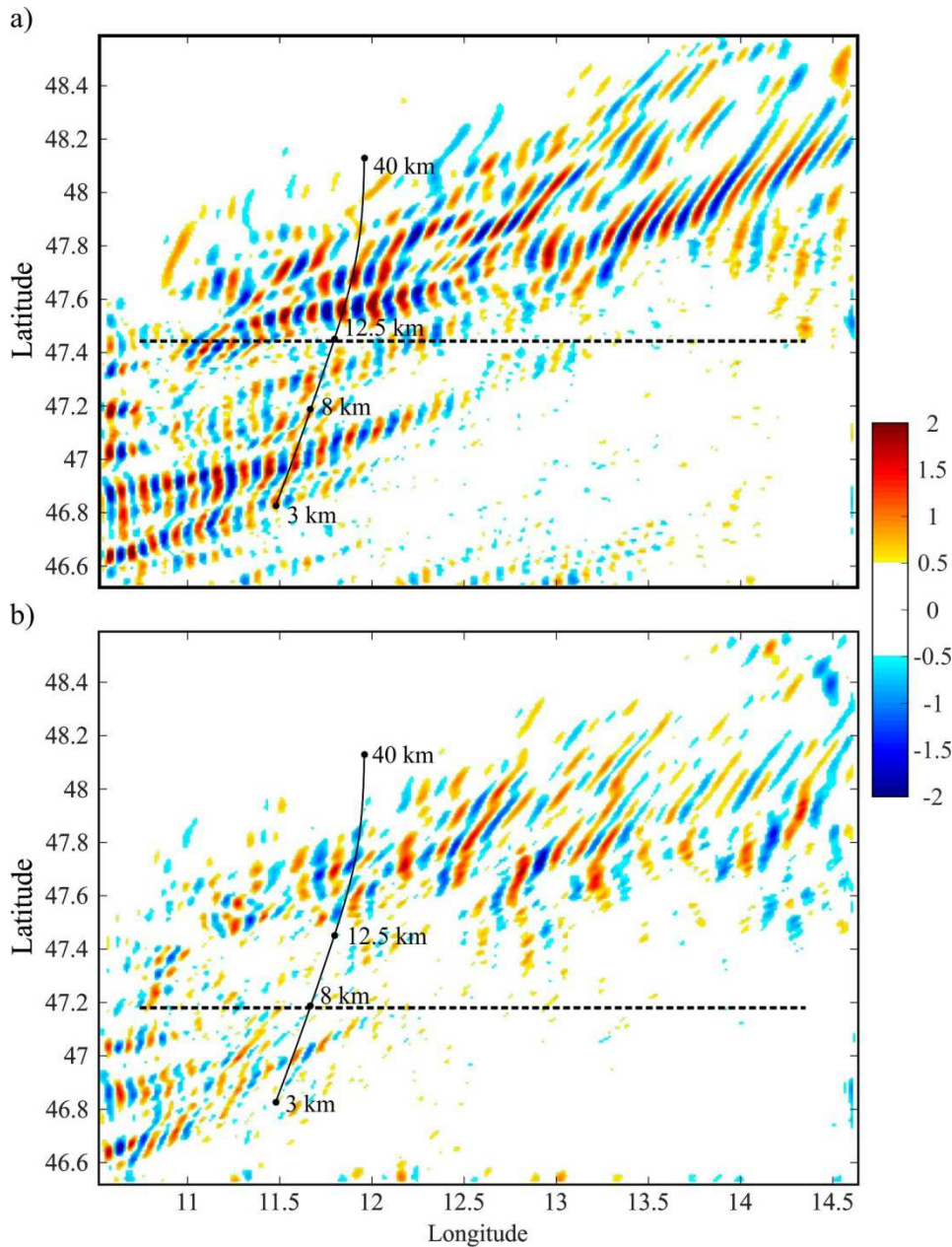
Figure 4: Simulated high resolution (inner WRF domain) δw structures at the Alps region (defined in Fig. 1). Two altitude levels, a) above and b) below the clouds top are shown. The line of tangent points (LTP) corresponding to the collocated RO event is indicated in both panels from lower (3 km) to upper (40 km) points (solid black line). The line of sight (LOS, dotted black line) at both levels is also indicated.

The mesoscale outputs were obtained every 60 min. It is generally accepted that δw adequately highlights the main GW amplitudes and wavelengths characteristic of MW. These, usually belong to high and medium intrinsic frequency regimes. In Fig. 4, coherent, mostly bi-dimensional GW structures with constant phase surfaces are seen. They are mainly oriented along S-N direction and slightly tilted to N-E with increasing latitude. The mean horizontal wind is directed from NW to SE at 700 hPa, causing the apparent forcing of MW. It is equal to $[U,V] = [3;-3]$ m/s at 18 UTC. Prevailing amplitudes and λ_H ranging between 1-2 m s^{-1} and 20-60 km respectively are distinguished. Two main features may be remarked at both levels. GW amplitudes are weaker below than above the cloud tops and two different

structures are visible. One structure is stationary and the other is not stationary. The last one is zonally and meridionally displaced when observed at 1-hour intervals during the evolution of convection (not shown). The GW sources seem to be orographic forcing and associated to the clouds development respectively. δw amplitude values up to 2 m s^{-1} correspond to MW with short horizontal wavelength. These δw perturbations exhibit, as expected, the presence of MW more clearly than δT. (Fig 5a). Contrarily, the non stationary GW with longer λ_H and amplitude values above 2 K are more evident in δT than in δw, as a function of longitude and latitude (Fig 5b and 5c). Systematic λ_Z values ~ 8 km, associated to these longer λ_H are appreciated. In these figures, the vertical line indicates the position of the RO mean TP. The orographic amplitudes are more significant early in the morning, exhibiting a general decrease with increasing local time (not shown). They reach large amplitudes at stratospheric heights beyond the tropopause, located at 11 km. No critical levels for MW or reflection effects are observed (Fig.5d). The strongest orographic structures are observed until the early afternoon. On the other hand, the non-stationary GW packets are generated between 12 km and 17 km height, during the convection development after mid-afternoon and radiated above the cloud tops. The longer λ_H values are not well defined, suggesting the coexistence of two or more non-stationary modes.
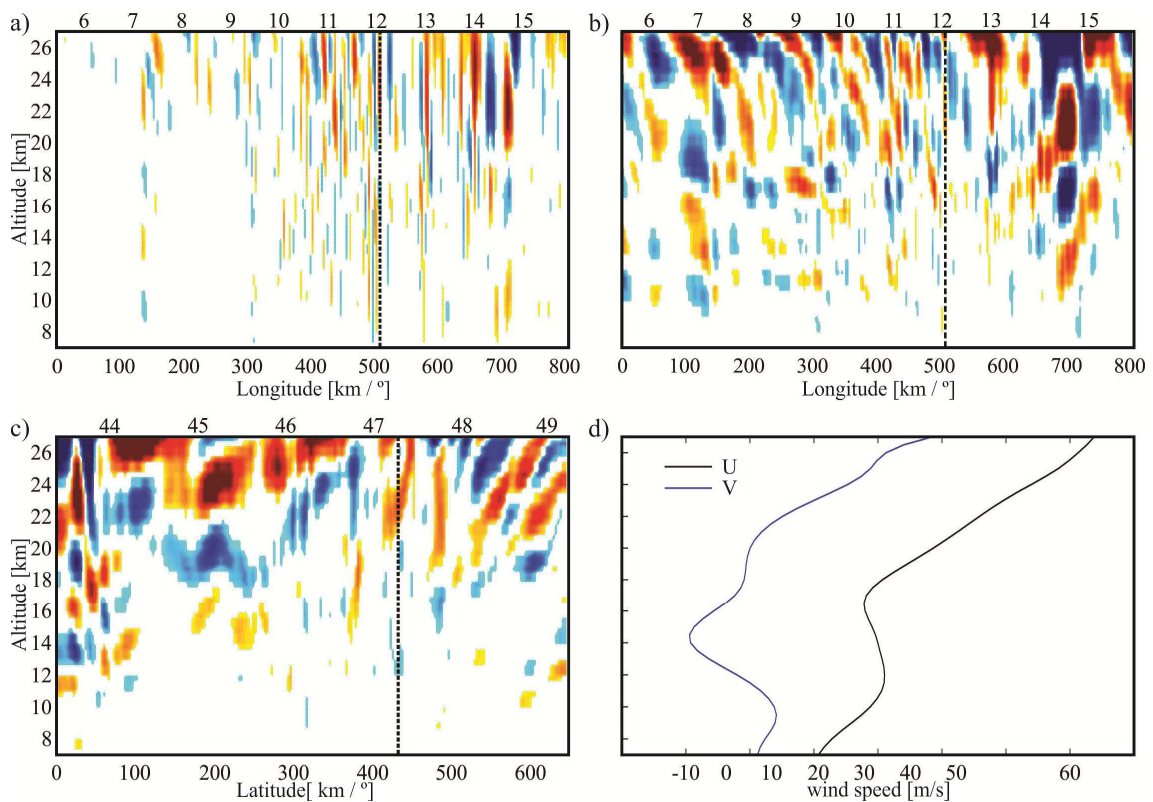
Figure 5. Simulated high resolution GW structures at the Alps region, showing a) δw and δT signatures as a function of b) longitude and c) latitude. Non-stationary/stationary GW with longer/shorter horizontal wavelength are more clearly seen in $\delta T/$ δw. d) Zonal and meridional mean wind. The dotted line indicates the position of the TP.

3.1.2. Analysis of gravity waves in the RO observation

The wavelike structure of the RO *T* profile, retrieved at the Alps region is analyzed. This profile is shown in the central panels of Fig 3a. Its horizontally projected line of tangent points (LTP) is seen in Fig. 4.

265
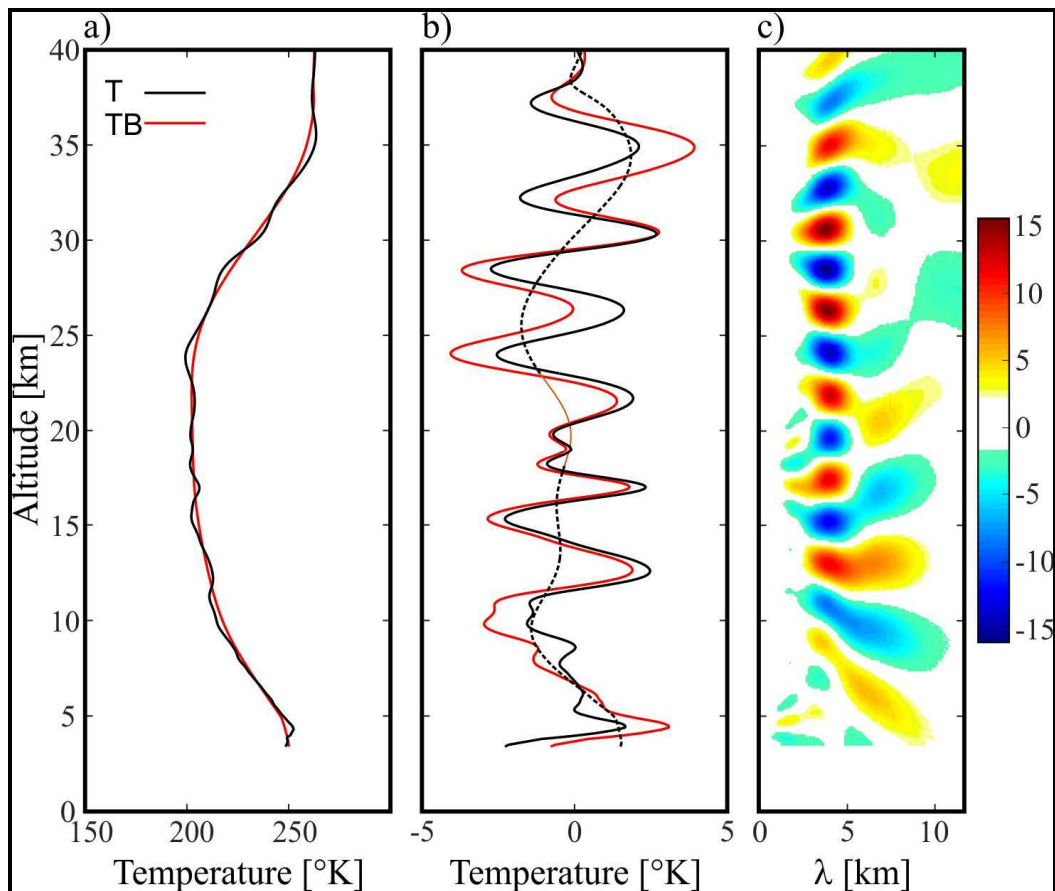
Figure 6: a) Retrieved RO *T* vertical profile (black line) and its corresponding low-pass background component *TB* (red line) at the Alps region. b) Remaining oscillation (black), isolated after applying a band-pass filter (red) and a double filtering process to the background (black dotted) profile. c)
270 Continuous wavelet transform (CWT) applied to the perturbation *T* structure, as a function of the vertical wavelength. The RO event took place at 17:24 UTC.

In doing so, the perturbation component of this profile is removed (Fig. 6a). If a simple band-pass filter is applied (e.g., de la Torre et al, 2006), the "tropopause problem" must be faced, as far as RO *T* profiles are available as a function of altitude. As pointed out by Alexander et al. (2011), even if filters with ideal cut-
275 offs exist, part of the problem would still be there because the tropopause kink usually departs from a sinusoid or any other function that may be used as a basis. Real filters do not yield ideal spectral component isolations (side effects are amplitude reduction for example) and may need some manual fine tuning procedures to optimize their performance. After a "perfect" band-pass is used, there should be no remaining components at wavelengths outside the considered range. The method here applied consists in
280 two steps. (i) A bandpass filtering to isolate the wavelength range of interest to separate the background and eliminate the noise was used. (ii) A cutoff larger than or equal to the bandpass upper limit was applied. This allows to remove large wavelengths representing background behavior or trends still present

and to force a zero mean. The tropopause kink in T can be viewed as the surrounding of a long sinusoidal peak. In the first step, a bandpass between 1 km and 10 km, and in the second step, a cutoff of 10 km are applied. The resulting filtered δT profile is marked by the solid black line in Fig. 6b. A continuous wavelet transform (CWT) is finally applied to the remaining δT wave structure (Fig. 6c).

The CWT is a useful method to detect the main oscillation modes present in a signal analysis. As it is known, it is a powerful tool for studying multiscale and non-stationary processes occurring over finite spatial and temporal domains (Lau and Weng, 1995). It allows detecting short-period as well as long-period oscillations. The CWT compares the original signal against a set of synthetical signals, which are called mother wavelets, obtaining correlation coefficients. The comparison between signals is carried out through a process of translation and contraction or dilation of the mother wavelet in each signal portion. This process is repeated for all scales of mother wavelets, allowing the location of short life and high-frequency signals like sharp changes, thus obtaining detailed information. In this work, the mother wavelet selected is the Morlet wavelet (Morlet, 1983), which consists of a flat wave modified by a Gaussian envelope. Fig. 6c shows a clear GW signal throughout the tropo-stratospheric region, with prevailing $\lambda_Z = 4$ km. A second considerably weaker mode is also present in the troposphere, with λ_Z close to 7 km.

To search for a possible correspondence among these two modes and the structures observed in Figs. 4 and 5, the expected amplitude attenuation effects must be considered (P. Alexander et al., 2008). In particular, for this RO event, the LOS stands at each TP almost exactly perpendicular to the GW phase surfaces observed in Fig. 3, at 88° from North direction (dotted lines in Fig. 4). This should prevent the observation of vertical oscillations corresponding to short λ_H structures, as seen in Fig. 4. In this figure, the quasi perpendicular orientation of the constant GW phases relative to the line of sight (LOS) is appreciated. This clearly does not benefit the GW detection during the RO event. The horizontal averaging of RO retrievals produces an amplitude attenuation and phase shift in any plane GW, which may lead to significant discrepancies with respect to the original values (Alexander et al., 2008). The lower and upper altitudes of LTP are 3 km and 40 km, respectively. The observation of GW structures with short λ_H observed in Fig. 4, will expectedly suffer amplitude attenuation and should not be visible by GPS RO events (Preusse et al., 2002; P. Alexander et al., 2008). An estimation of the expected attenuation in the stationary and non stationary structures during the RO sounding is performed. The amplitude attenuation factor defined as the ratio between derived and original amplitudes is deduced. This factor is a function of the ratio of GW vertical and horizontal wavelengths and the angle on the horizontal plane between the wave fronts and the line of sight (LOS). Ideal conditions that lead to no attenuation are, respectively, a null ratio between vertical and horizontal wavelengths and a null angle between LOS and the fronts. The analyzed case study shows the corresponding values of both parameters and the attenuation factor (range 0-1 covers from null to full output) (Table 1). According to these results, in the Alps case study a considerable attenuation of mountain waves below the tropopause is expected.

3.1.3. Analysis of GW structures from ERA Interim data.

320   The resulting estimation of a negligible attenuation factor at both height levels shown in Fig. 4, confirms that the GW cannot be captured there during the RO event. It is clear that the mesoscale simulations are not enough to explain the observed GW structure. To understand the origin of the oscillation observed in the RO δT profile, the possibility that the presence of GW with scale long enough is not able to be captured by mesoscale WRF simulations is analyzed. According to this, the corresponding ERA Interim

325   reanalyses data are observed. In Fig. 7, δT resulting from these data at 22 km height reveals a defined non-stationary oscillation propagating in NW-SE direction, with λ_X and λ_Y equal to 530 and 650 km respectively. The attenuation factor derived from these values is estimated in 0.90. This value is consistent with a clear oscillation observed at stratospheric heights in the RO profile, with λ_Z equal to 4 km (Fig. 6c and Table 1).

330
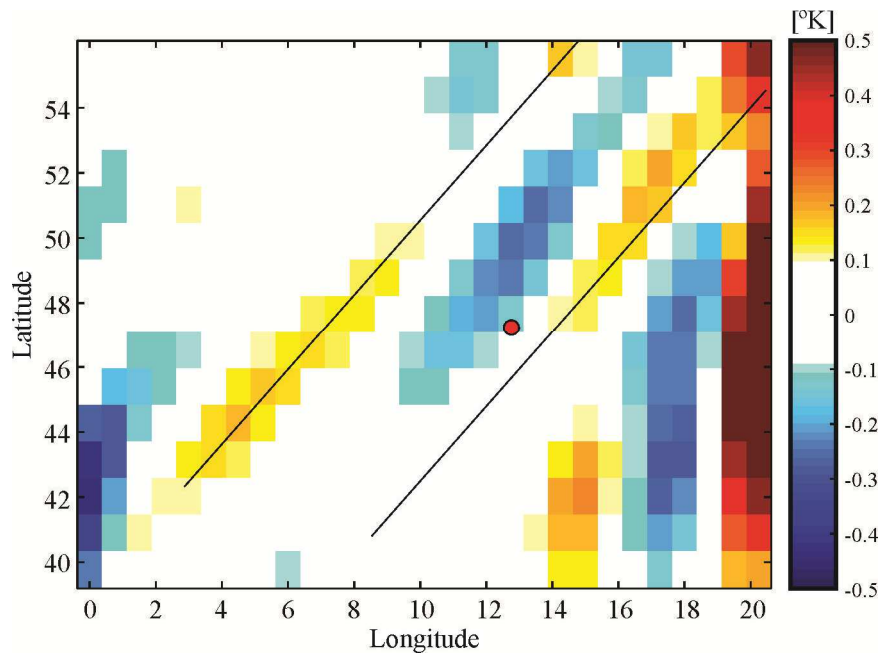
Figure 7. ERA Interim δT data corresponding to the case study at the Alps region. The red point indicates the mean TP

335

vertical/horizontal   angle between   attenuation

	wavelength ratio	wave fronts and LOS	factor
Alps above	0.02	48	0.90
Alps below	0.51	78	1e-49
Andes above	0.01	32	0.99
Andes below	0.35	7	0.44

340   Table 1. Attenuation factor as a function of the ratio of GW vertical and horizontal wavelengths and the angle, on the horizontal plane, between the wave fronts and the LOS. Alps and Andes case studies above and below the tropopause level. A considerable/partial attenuation below the tropopause at the Alps/Andes region is expected.

Independently to the expected attenuation, an additional distortion must be considered due to the slanted
345   nature of the sounding. This is introduced in the measured GW λ_H and λ_Z by atmospheric soundings performed in any other than vertical and horizontal direction. This is the case during GPS RO events or during radiosoundings (e.g., de la Torre and Alexander, 1995; P. Alexander et al., 2008). In the case of RO events, a visibility condition imposed to the line of sight (LOS) described in P. Alexander et al. (2008), must be satisfied. The distortion is more or less significant, depending on the elevation angle of
350   the sounding path and the GW aspect ratio (de la Torre et al., 2018, hereafter referred to as T18). For example, during vertically directed measurements with a single lidar, λ_H cannot be detected but λ_Z is not distorted. A clear advantage of numerical simulations or reanalyses data is that they are not affected by this systematic error inherent to any slanted atmospheric measurement. According to this, we must distinguish between "apparent" (i.e., RO observations) and "real" λ_H and λ_Z values. For this reason, the
355   apparent 4 km oscillation observed in Fig. 6c must be carefully observed as a distorted signature, which in fact corresponds to a different real λ_Z value (T18). Considerable under- or overestimations are in the general case expected, depending on the aspect ratio of GW and inclination of the LTP (T18 and Appendix).

360

365

3.2. Case study at the Andes region

3.2.1. *Numerical simulations of GW structures*

370 From the simulated dynamic and thermodynamic parameters, in Fig. 8 we show δw at constant height levels for the Andes area, delimited in Fig. 1. Constant altitudes of 10 km, 16 km, below (Fig. 8a) and above (Fig. 8b) the cloud top (situated at 14 km height), respectedly, and at 26 km (Fig. 8c), at 17:00 UTC, are selected. The δw field is represented a few minutes before the RO event (16:56 UTC).
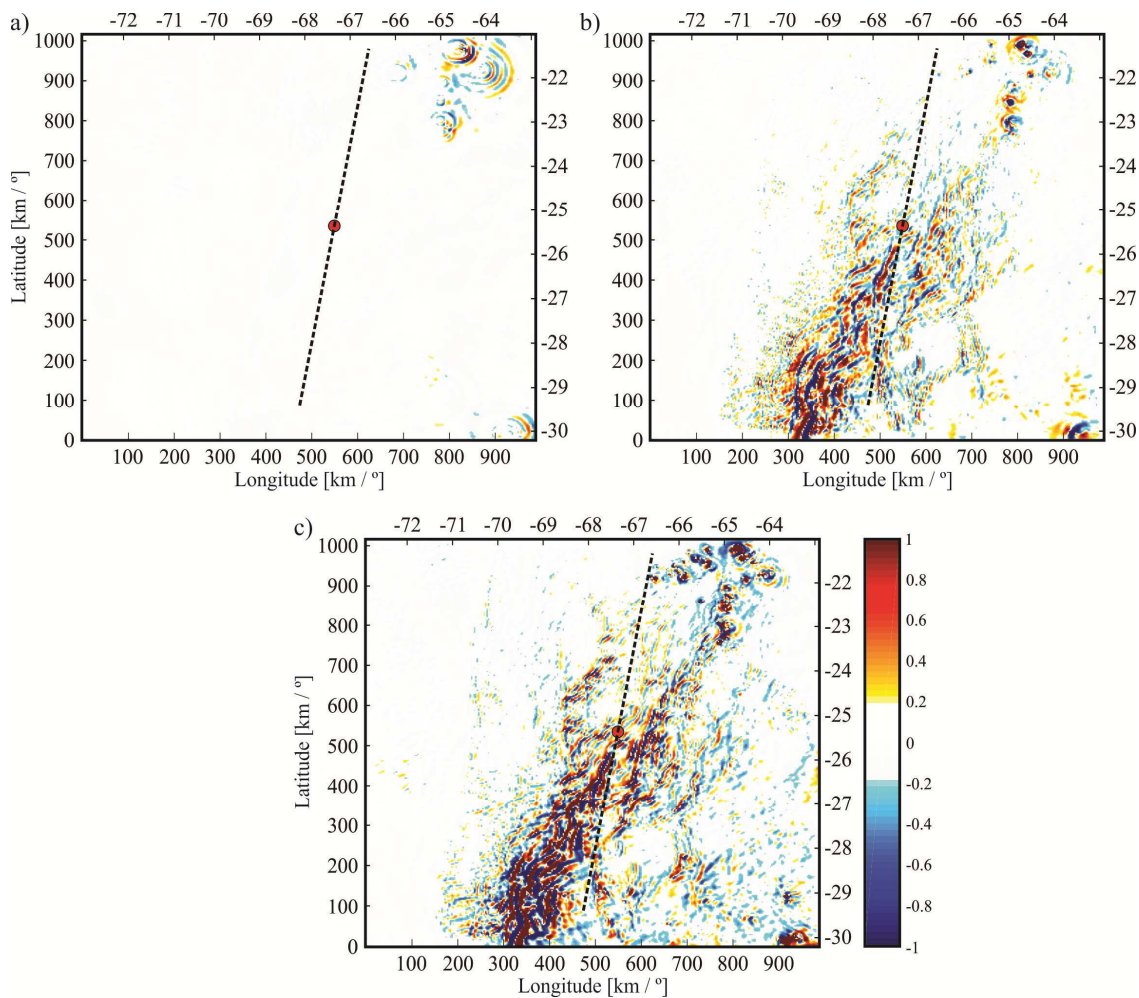
Figure 8: Simulated high resolution GW structures in the Andes region delimited in Fig. 1. Three constant
375 altitudes, a) at 26 km, b) at 16 km (above) and c) at 10 km (below) the cloud tops (situated at 14 km) are selected. In this case, the mean LTP (black line) is located around 25.5°S and 67.1°W. The TP altitudes. The red point indicates the mean TP. The dotted line indicates the LOS crossing the TP corresponding to each selected altitude.

Coherent bi-dimensional GW structures with constant phase surfaces oriented from SW to NE are seen
380 (Fig 8a and 8b). The mean horizontal wind vector at 700 hPa directed from NW to SE is [U,V] = [7;-3] m/s at 18 UTC. de la Torre et al. (2015) have shown that immediately to the south of Central Andes, close

to the mountain tops, two clearly different orographic GW structures are systematically observed at constant pressure levels. One structure type shows highly elongated alternating positive and negative parallel δw bands, aligned almost in N-S direction. The second type presents a bi-dimensional distribution too, but exhibits alternating fringes of much shorter longitude, mostly in SW–NE direction. The mean wind that forces mountain waves exhibiting the 1D structures of the first type, presents an intense zonal gradient of zonal wind, veering to an increasing westerly mean wind with increasing latitude. The meridional wind component is usually negligible. In the 2D structures of the second type, at and below mountain top levels, a prevailing intense negative meridional wind with less zonal wind contribution is observed. In the case study shown in Fig. 8, the mean wind at 700 hPa with considerable negative meridional component, is associated to the second type. In Fig. 8a to 8c, additional orographic GW structures situated at the NE and SE of the domain are observed. They propagate from low altitudes until at least the upper limit of the simulations. These structures exhibit stationary circularly shaped wave fronts. They penetrate beyond the critical layer for orographic GW, situated at an almost zero wind level, near to 18 km height (Fig. 8a to 8c and 9d).

In Fig. 9a to 9c, as in the Alps case, δw perturbations exhibit the presence of mountain waves more clearly than δT. (Fig 9a). Nevertheless, in Fig 9b and 9c, the presence of two different GW structures, separated by a critical layer at 18 km as a function of longitude and latitude, is identified. The MW propagate upwards and just below the critical layer they increase their amplitude, with decreasing λ_Z in agreement with linear GW theory. Inversely to the Alps case study, the orographic amplitudes at the Andes region are more significant in the afternoon. They exhibit a general increase since sunrise with increasing local time. Above the critical layer, non-stationary GW packets are generated during the convection development after mid-afternoon and radiated above the cloud tops. These longer λ_H values are well resolved by WRF and shorter from the simulations, than in the Alps case study. In the Andes case, there is almost no spatial coexistence between GW from both GW sources. A clear separation between orographic structures below the critical layer and convective GW above it, is quite evident.
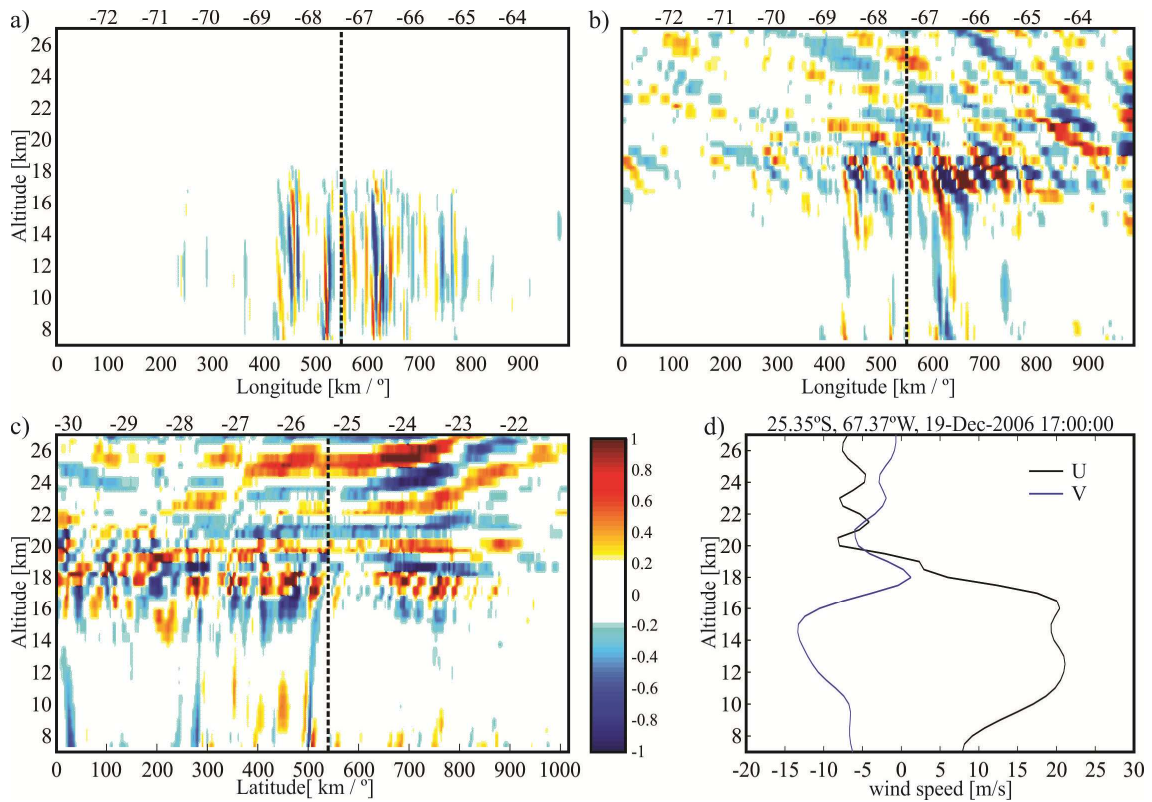
410   Figure 9. Simulated high resolution GW structures at the Andes region, showing a) δw and δT signatures
as a function of b) longitude and c) latitude. Non-stationary/stationary GW with longer/shorter horizontal
wavelength and shorter/longer vertical wavelength, above/below the critical layer are appreciated. d)
Zonal and meridional mean wind.

415

Next, the wavelike structure of the RO T profile, retrieved at the Andes region. This profile is shown in
the central panels of Fig 3b. Its horizontally projected LTP is seen in Fig. 8, is analyzed.

420

3.2.2. *Analysis of gravity waves in the RO observation*

425

The procedure is identical to the one applied in case study 1.The utility of the double filter applied is more obvious here than in the Alps case study. Also, the tropopause kink is sharper (Fig. 10b). For this RO event, inversely to the described situation in the Alps case study, the LOS stands at each TP almost aligned to the GW phase surfaces observed in Fig. 8, at 190° from north direction (dotted lines in Fig. 8).

430 This may allow us to detect vertical oscillations in the RO profile corresponding to the short λ_H MW structures seen below the critical layer in Fig. 8 and 9.
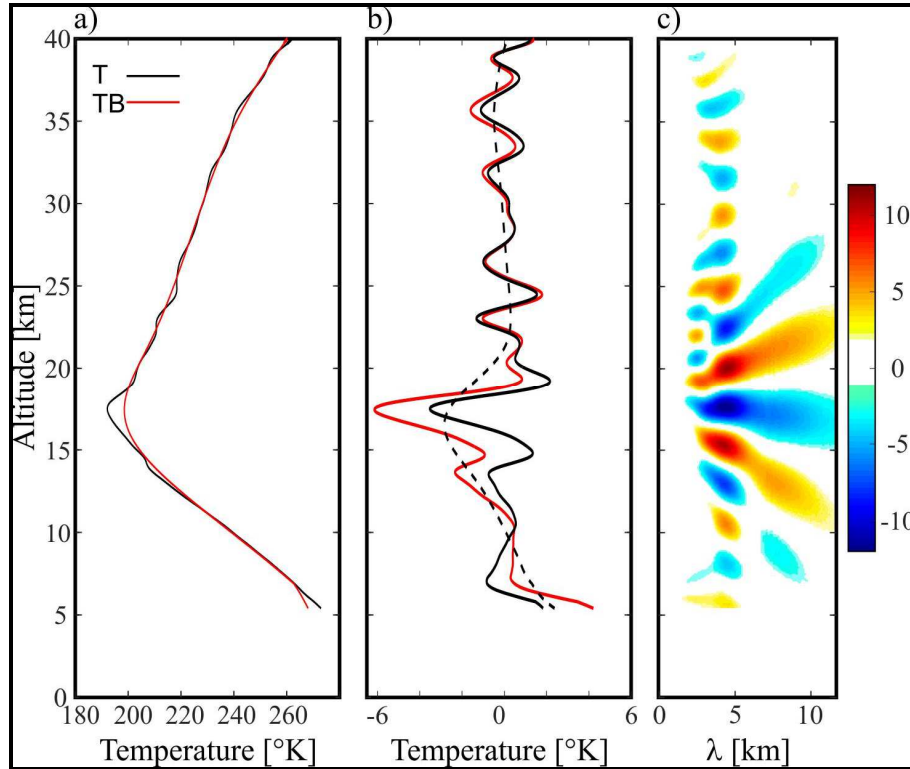
Figure 10: The same as in Fig. 6, here for the case study at the Andes region.

435 In Fig. 10c, a clear GW signal appears also in the Andes case, propagating throughout the tropo-stratospheric region with a prevailing $\lambda_Z = 4.5$ km. Here again, attenuation and distortion effects must be considered. The computation of a partial attenuation factor (0.44, Table 1) at the troposphere confirms that the mountain waves at these levels can be captured during the RO event. In this estimation, λ_X, λ_Y and λ_Z values equal to 30, 100 and 10 km respectively are considered. In this case study, the mesoscale

440 simulations are enough to explain the observed GW structure above the critical layer too. Clear signatures of λ_X, λ_Y and λ_Z equal to 350, 400 and 3 km respectively may be seen. These values yield a very high attenuation factor (0.99). To understand the origin of the oscillation observed in the RO δT profile, we conclude that below the tropopause, the oscillation is completely due to orographic waves and above, to convective GW. In both cases, mesoscale simulations were able to capture the GW structures. In this case

445 study, like in the Alps case, an expected distortion in the measured λ_Z value, due to the slanted nature of the sounding must be expected too.

450

$$\lambda_Z^{ap} = \frac{\lambda_Z}{abs(1 + \cot(\alpha)\cot(\psi))} \quad D = \frac{\lambda_Z^{ap}}{\lambda_Z}$$

4. Conclusions From an initial set of collocations between convective systems and GPS RO observations,
455 the applicability of these data sets for the detection and investigation of convective systems and GW over orographic regions is analyzed. In doing so, mountain regions of Europe and South America, over sub-tropical to mid-latitude regions, the Alps and Andes ranges, are selected. A collocation database was built up. We use RO bending angle and T profiles retrieved at the Wegener Center with processing version OPSv5.6. The storm systems are located in time and space according to the global deep convective
460 tracking database ISCCP. From an initial set of 294 and 50 collocations at Alps and Andes regions respectively, a subset of 10 collocations are pre-selected. This pre-selection is based on the observation of large amplitudes, presumably GW, in the retrieved T RO profiles. Two case studies are finally studied in detail, at the Alps and Andes regions, respectively. The case studies are investigated using mesoscale WRF simulations, ERA Interim reanalyses data and the measured RO T profiles. The case studies
465 considered are selected based on the absence of jets and fronts, in order to be able to filter out two relevant possible sources of GW. Similar GW regimes and dominant vertical and horizontal wavelengths, from convective and orographic origin, are found at both regions. MW reach above the Alps higher altitudes than close to the Andes. The background mean wind above this last region imposes a critical level for mountain wave propagation, avoiding the propagation of GW packets up to stratospheric
470 heights.

At the Alps, mostly bi-dimensional GW structures with constant phase surfaces are seen. The mean horizontal wind cause the apparent forcing of MW. Prevailing amplitudes and λ_H ranging between 1-2 m s^{-1} and 20-60 km respectively are distinguished. GW amplitudes are weaker below than above the cloud tops and two different structures are visible. One structure is stationary and the other is not stationary. The
475 GW sources seem to be orographic forcing and associated to the clouds development respectively. δw amplitude values up to 2 m s^{-1} correspond to MW with short horizontal wavelength. These δw perturbations exhibit, expectedly, the presence of MW more clearly than δT. Contrarily, the non stationary GW with longer λ_H and amplitude values above 2 K are more evident in δT than in δw. Systematic λ_Z values close to 8 km, associated to these longer λ_H are appreciated. The orographic
480 amplitudes are more significant early in the morning, exhibiting a general decrease with increasing local time. They reach large amplitudes at stratospheric heights beyond the tropopause, located at 11 km. No critical levels or reflection effects are observed. The strongest orographic structures are observed until the early afternoon. The non-stationary GW packets are generated during the convection development after

mid-afternoon and radiated above the cloud tops. The longer λ_H values are not well defined, suggesting the coexistence of two or more non-stationary modes. From the RO profile, the perturbation component is removed, considering the tropopause obstacle to filter out the wavelike structure. A CWT is applied to the remaining δT. A clear GW signal throughout the tropo-stratospheric region, with prevailing $\lambda_Z = 4$ km is found. The correspondence between these two modes and the structures observed in the simulations are investigated. In doing so, the expected amplitude attenuation effects in the RO sounding are considered. It is concluded that the LOS and the wavelength ratio should prevent for the observation of vertical oscillations corresponding to short λ_H structures. This clearly does not benefit the GW detection during the RO event. The horizontal averaging of RO retrievals produces an amplitude attenuation and phase shift in any plane GW, which may lead to significant discrepancies with respect to the original values. An estimation of the expected attenuation in the stationary and non stationary structures during the RO sounding is performed. The amplitude attenuation factor defined as the ratio between derived and original amplitudes is deduced. Ideal conditions that lead to no attenuation are, respectively, a null ratio between vertical and horizontal wavelengths and a null angle between LOS and the fronts. The analyzed case study shows the corresponding values of both parameters and the attenuation factor. In this Alps case study a considerable attenuation of mountain waves below the tropopause is expected. The resulting estimation of a negligible attenuation factor in the troposphere confirms that the GW cannot be captured there during the RO event. As the mesoscale simulations are not enough to capture and explain the observed GW structure the corresponding ERA Interim reanalyses data are observed. From these data at 22 km height, a defined non-stationary oscillation propagating in NW-SE direction with λ_X and λ_Y equal to 530 and 650 km respectively is observed. This explains the oscillation seen in the RO δT profile.

At the Andes, coherent bi-dimensional GW structures with constant phase surfaces oriented from SW to NE, of a type already reported in a previous work, are seen. Additional orographic GW structures situated at the NE and SE of the domain are observed. They propagate from lower altitudes until at least the upper limit of the simulations. These structures, exhibit stationary circular wave fronts and penetrate beyond the critical layer for orographic GW, situated at an almost zero wind level, near to 18 km height..As in the Alps case, δw perturbations exhibit the presence of MW more clearly than δT. The presence of two different GW structures, separated by a critical layer at 18 km is identified. The MW propagate upwards and just below the critical layer they increase their amplitude, decreasing λ_Z. Inversely to the Alps case study, the orographic amplitudes at the Andes region are, as usually, more significant in the afternoon, exhibiting a general increase with increasing local time. Above the critical layer, non-stationary GW packets are generated during the convection development after mid-afternoon and radiated above the cloud tops. In this case, there is almost no spatial coexistence between GW from both GW sources.

In the retrieved RO δT profile a signal appears also propagating throughout the tropo-stratospheric region with a prevailing $\lambda_Z = 4.5$ km. A partial attenuation reveals that at the troposphere, MW can be captured during the RO event. In this estimation, λ_X, λ_Y and λ_Z values equal to 30, 100 and 10 km respectively are considered. In this case study, the mesoscale simulations are enough to explain the observed GW structure above the critical layer too. Clear signatures of λ_X, λ_Y and λ_Z equal to 350, 400 and 3 km respectively may be seen. These values yield a very high attenuation factor (0.99). It is concluded that

below the tropopause, the oscillation is entirely due to orographic waves and above, to convective GW. In both cases, mesoscale simulations were able to capture the GW structures. In this case study like in the Alps case, additionally, an expected distortion in the measured λ_Z value must be also forseen. This is due to the slanted nature of the sounding and depends on the GW aspect ratio too.

530

Apendix

The discrepancy between measured and simulated λ_Z (an analogous discussion could be given regarding λ_H, too –see T17-) may be quantitatively explained as follows. It may be assumed that RO soundings yield T profiles almost instantaneously in such a way that GWs are "frozen" in space during the entire LTP retrieval. The vertical "real" and "apparent" (or measured) wavelengths (λ_z and λ_z^{ap}, respectively) are related according to the following expression (T18):

$$\lambda_Z^{ap} = \frac{\lambda_Z}{abs(1 + \cot(\alpha)\cot(\psi))} \quad \text{(A1)}$$

where α is the elevation angle, defined by a straight sounding path direction and the horizontal plane, and $\cot(\psi)$ is the ratio between the horizontal wavenumber vector (k_H) projected on the vertical plane containing the LTP, and the vertical wavenumber k_Z. The ratio $k_H/k_Z = \lambda_Z/\lambda_H$ is also known as the GW aspect ratio = tg (ψ). It is defined the distortion as the ratio:

$$D = \frac{\lambda_Z^{ap}}{\lambda_Z} \quad \text{(A2)}$$

and plot this parameter, following Eq. (A1), as a function of α and ψ (red line in Fig. A1). For the LTP shown in Fig. 8, considering that both the horizontal and vertical excursion of LTP, as well as the upper and lower altitudes (40 and 3 km), are known, we infer an average $\alpha = 0.68$ rad. A different curve is obviously expected for different α values, althought fitting a similar shape. The divergence at high D values is only suggested by plotting its variability up to $D = 5$. The left green circle qualitatively indicates the D-ψ GPS RO sector encompassing the functional relation among the 3 parameters. The right green circle is included, because an uncertainty beween α and $\pi-\alpha$ for our estimated aspect ratio still remains from our previous estimation. The white, light grey and grey backgrounds indicate, for reference purposes, the non-hydrostatic, hydrostatic non-rotating and hydrostatic rotating GW regimes, respectively. Both quadrants are separated by a vertical dashed curve. The horizontal dashed line represents the non-distortion limit, where λ_Z and λ_Z^{ap} should coincide. According to both possibilities (the internal regions defined by any of the green circles), in the case considered (Fig. 10c), there are two

possibilities indicating an under- and an overestimation of λ_Z respectively. This uncertainty can be removed by inspection of Fig. 10 (see T18).
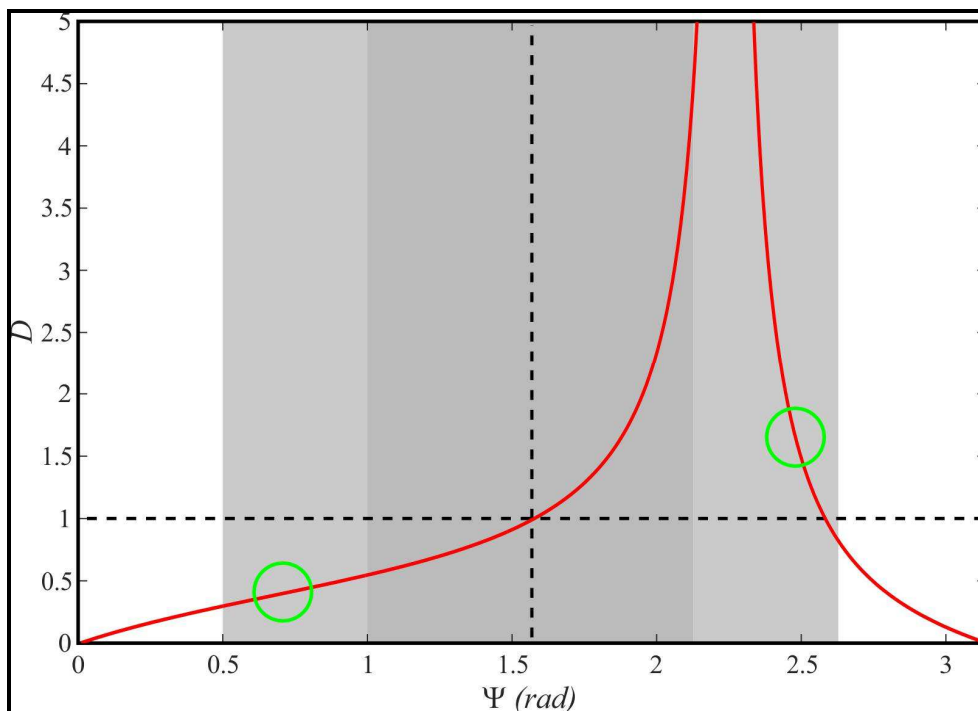
Figure A1: Distortion expected between measured and simulated λ_Z (green circles) regarding the GW
560 parameters derived from the GPS RO event above the Andes, as detailed in Figs. 8, 9 and 10. Both green circles illustrate possible combinations of the parameters for under- and overestimation of λ_Z.

5 Data availability

The WEGC OPSv5.6 RO dataset is available on request from WEGC and will be made publicly available
565 soon.Data on convective systems used in this study are available from the global deep convective tracking database of the International Satellite Cloud Climatology Project (ISCCP) via <https://isccp.giss.nasa.gov/CT/>. Cloud data from METEOSAT are available from the EUMETSAT processing centre via https://eoportal.eumetsat.int/userMgmt/login.faces and data from GOES are available from NOAA via https://www.class.ncdc.noaa.gov/saa/products/welcome.

570

Author contributions.

R. Hierro, A. de la Torre, A.K. Steiner, P. Alexander and P. Llamedo made the study design, performed the computational implementation and analysis, performed the numerical modelling, created the figures, and wrote the first draft of the paper.

575 A.K.Steiner provided guidance on RO data and analysis aspects and contributed to finalizing the manuscript.

P. Cremades provided recommendations and assistance in the WRF simulations.

Competing interests. The authors declare that they have no conflicts of interest.

580

Acknowledgements. We are grateful to R. Biondi (ISAC-CNR, Rome, Italy) for advice on cloud data and provision of the cloud detection algorithm and the reference climatology. We thank H. Truhetz (WEGC, Graz, AT) for help on WRF model aspects. We acknowledge UCAR/CDAAC (Boulder, CO, USA) for the provision of level 1a RO data and ECMWF (Reading, UK) for access to its analysis, and short-term forecast data. We thank the WEGC processing team members, especially M. Schwärz (WEGC, AT), for OPSv5.6 RO data and his special support. This study wasinitiated by the Programme of Exchange and Cooperation for International Studies between Europe and South America (PRECIOSA) by funding a research visit of R. Hierro at WEGC (University of Graz, Graz, AT). Part of the cooperation work wassupported by the Austrian Science Fund (FWF) under research grant P27724-NBL (VERTICLIM). The study has been supported by the CONICET under grants CONICET PIP11220120100034 and ANPCYT PICT 2013-1097.

585

590

References

Alexander, M. J.: The gravity wave response above deep convection in a squall line simulation, J. Atmos. Sci., 52, 2212–2226, 1995.

595

Alexander, P., de la Torre, A., Llamedo, P.: The interpretation of gravity waves signatures extracted from GPS radio occultations. *J. Geophys. Res.*, *113*, D16117, doi:10.1029/2007JD009390, 2008.

Alexander, P., de la Torre, A., Llamedo, P., Hierro, R., Schmidt, T., Haser, A., and Wickert., J.: A method to improve the determination of wave perturbations close to the tropopause by using a digital filter, Atmos. Meas. Tech., 4, 1777–1784, doi:10.5194/amt-4-1777-2011, 2011.

600

Angerer, B., Ladstädter, F., Scherllin-Pirscher, B., Schwärz, M., Steiner, A. K., Foelsche, U., and Kirchengast, G.: Quality aspects of the Wegener Center Multi-Satellite GPS Radio Occultation Record OPSv5.6, Atmos. Meas. Tech. Discuss., https://doi.org/10.5194/amt-2017-225, in review, 2017.

Barthlott, C., Corsmeier, U., Meißner, C., Braun, F., and Kottmeier, C.: The influence of mesoscale circulation systems on triggering convective cells over complex terrain, Atmos. Res.,81, 150–175, 2006.

605

Beres, J. H., Alexander, M. J., and Holton, J. R.: Effects of tropospheric wind shear on the spectrum of convectively generated gravity waves, J. Atmos. Sci., 59, 1805–1824, 2002.

Bica, B., Knabl, T., Steinacker, R., Ratheiser, M., Dorninger, M., Lotteraner, C., Schneider, S., Chimani, B., Gepp, W., and Tschannett, S.: Thermally and Dynamically Induced Pressure Features over Complex Terrain from High-Resolution Analyses, J. Appl. Meteor. Climatol., 46, 50–65, doi: 10.1175/JAM2418.1, 2007.

610

Biondi, R., Neubert, T., Syndergaard, S., and Nielsen, J. K.: Radio occultation bending angle anomalies during tropical cyclones, Atmos. Meas. Tech., 4, 1053-1060, doi:10.5194/amt-4-1053-2011, 2011.

Biondi, R., Randel, W. J., Ho, S.-P., Neubert, T., and Syndergaard, S.: Thermal structure of intense convective clouds derived from GPS radio occultations, Atmos. Chem. Phys., 12, 5309-5318, https://doi.org/10.5194/acp-12-5309-2012, 2012.

Biondi, R., Steiner, A. K., Kirchengast, G., and Rieckh, T.: Characterization of thermal structure and conditions for overshooting of tropical and extratropical cyclones with GPS radio occultation, Atmos. Chem. Phys., 15, 5181-5193, doi:10.5194/acp-15-5181-2015, 2015.

Biondi, R., Steiner, A. K., Kirchengast, G., Brenot, H., and Rieckh, T.: Supporting the detection and monitoring of volcanic clouds: a promising new application of Global Navigation Satellite System radio occultation, Adv. Space Res., 60, in press. DOI:10.1016/j.asr.2017.06.039, 2017.

Clark, T. L., Hauf, T., and Kuettner, J. P.: Convectively forced internal gravity waves: Results from two-dimensional numerical experiments, Q. J. R. Meteorol. Soc., 112, 899–925, doi:10.1002/qj.49711247402, 1986.

de la Torre, A., and P. Alexander: The interpretation of wavelengths nd periods as measured from atmospheric balloons, J. Appl. Meteorol., 34, 2747– 2754, 1995.

de la Torre, A., V. Daniel, R. Tailleux, and H. Teitelbaum: A Deep Convection Event above the Tunuyán Valley near the Andes Mountains. Mon. Wea. Rev., 132, 2259–2268, https://doi.org/10.1175/1520-0493(2004)132<2259:ADCEAT>2.0.CO;2, 2004.

de la Torre A., Alexander, P., Llamedo, P., Menéndez, C., Schmidt, T., and Wickert, J.: Gravity waves above andes detected from GPS radio occultation temperature profiles. II: jet mechanism?, Geophys. Res. Lett, 33, L24810, doi:10.1029/2006GL027343, 2006.

de la Torre, A., Hierro, R., Llamedo, P., Rolla, A., and Alexander, P.: Severe hail storms near southern andes in the presence of mountain waves, Atmos. Res., 101, (1-2), 112-123,dx.doi.org/10.1016/j.atmosres.2011.01.015, 2011.

de la Torre, A., Alexander, P., Hierro, R., Llamedo, P., Rolla, A., Schmidt, T., and Wickert, J.: Large amplitude gravity waves above the southern andes, the Drake passage and the Antarctic peninsula, J. Geophys. Res. (Atmosphere), 117, D02106, dx.doi.org/10.1029/2011JD016377, 2012.

de la Torre, A., Pessano, H., Hierro, R., Santos, R., Llamedo P., and Alexander, P.: The influence of topography on vertical velocity of air in relation to severe storms near the Southern Andes Mountains, Atmos. Res., 156, 91-101, dx.doi.org/10.1016/j.atmosres.2014.12.020, 2015.

de la Torre, A., Alexander, P., Schmidt, T., Llamedo and P., Hierro, R.: On the distortions in calculated GW parameters during slanted atmospheric soundings, Atmos. Meas. Tech., in press.

Demko, J. C., Geerts, B., Miao, Q., and Zehnder, J. A.: Boundary layer energy transport and cumulus development over a heated mountain, an observational study, Mon. Wea. Rev., 137, 447–468, 2009.

Dutta, G., Ajay Kumar, M. C., Vinay Kumar, P., Venkat Ratnam, M., Chandrashekar, M., Shibagaki, Y., Salauddin, M., and Basha, H. A.: Characteristics of high-frequency gravity waves generated by tropical deep convection: Case studies, J. Geophys. Res., 114, D18109, doi:10.1029/2008JD011332, 2009.

650   Eckermann, S.D., Preusse, P.: Global measurements of stratospheric mountain waves from space. Science 286, 1534–1537, 1999.

Evan, S., Alexander, M.J., and Dudhia, J.: Model Study of intermediate-scale tropical inertia-gravity waves and comparison to twp-ice campaign observations, J. Atmos. Sci., 69, 591–610, doi: 10.1175/JAS-D-11-051.1, 2012.

655   Fovell, R., Durran, D., and Holton, J. R.: Numerical simulations of convectively generated stratospheric gravity waves, J. Atmos. Sci., 49, 1427–1442, doi:10.1175/1520 0469(1992)049<1427:NSOCGS>2.0.CO;2, 1992.

Fritts, D. C., Alexander. M.J.: Gravity wave dynamics and effects in the middle atmosphere, Rev. Geophys., 41(1), 1003, doi:10.1029/2001RG000106, 2003.

660   Grell, G.A., Devenyi, D.: A generalized approach to parameterizing convection combining ensemble and data assimilation techniques. Geophys. Res. Lett. 29. doi:10.1029/2002GL015311, 2002.

Hierro, R., Pessano, H., Llamedo, P., de la Torre, A., Alexander, P., and Odiard, A.: Orographic effects related to deep convection events over the Andes region, Atmos. Res., 120-121,216-225, dx.doi.org/10.1016/j.atmosres.2012.08.020, 2013.

665   Hong, S.-Y., Dudhia, J., Chen, S.-H.: A revised approach to ice microphysical processes for the bulk parameterization of cloud and precipitation. Mon. Weather Rev. 132, 103–120, 2004.

Hong, S.-Y., Noh, Y., Dudhia, J.: A new vertical diffusion package with an explicit treatment of entrainment processes. Mon. Weather Rev. 134, 2318–2341, 2006.

Houze, R. A.Jr.: Orographic effects on precipitating clouds, Rev. Geophys., 50, RG1001,
670   doi:10.1029/2011RG000365, 2012.

Kursinski, E. R. and Gebhardt, T.: A method to deconvolve errors in GPS RO-derived water vapor histograms, J. Atmos. Oceanic Technol., 31 (12), 2606–2628, doi:10.1175/JTECH-D-13-00233.1, 2014.

Kursinski, E. R., Hajj, G. A., Schofield, J. T., Linfield, R. P., and Hardy, K. R.: Observing Earth's atmosphere with radio occultation measurements using the Global Positioning System, J. Geophys. Res,
675   102(D19), 23429–23465, doi:10.1029/97JD01569, 1997.

Langhans, W., Schmidli, J., Fuhrer, O., Bieri, S., and Schär, C.: Long-Term Simulations of Thermally Driven Flows and Orographic Convection at Convection-Parameterizing and Cloud-Resolving Resolutions, J. Appl. Meteor. Climatol., 52, 1490–1510, doi:10.1175/JAMC-D-12-0167.1, 2013.

Lau, K.-M. and H. Weng: Climate signal detection using wavelet transform: How to make a time series
680   sing, Bull. Am. Meteorol. Soc., 76, 2391–2402., 1995.

Mlawer, E.J., Taubman, S.J., Brown, P.D., Iacono, M.J., Clough, S.A.: Radiative transfer for inhomogeneous atmosphere: RRTM, a validated correlated-k model for the long-wave. J. Geophys. Res. 102 (D14), 16663–16682, 1997.

Monin, A.S., Obukhov, A.M.: Basic laws of turbulent mixing in the surface layer of the atmosphere. Trans. Geophys. Inst. Akad. Nauk. USSR 151, 163–187, 1954.

Preusse, P., Dornbrack, A., Eckermann, S.D., Riese, M., Schaeler, B., Bacmeister, J.T., Broutman, D. and Grossmann, K.U.: Space-based measurements of stratospheric mountain waves by CRISTA: 1. Sensitivity, analysis method, and a case study, J. Geophys. Res., 107(D23), 8178, doi:10.1029/2001JD000699, 2002.

Morlet, J.: Sampling theory and wave propagation, in Acoustic Signal/Image Processing and Recognition, in NATO ASI, vol. 1, edited by C. Chen, 233–261, Springer-Verlag, New York., 1983.

Pandya, R. E. and Alexander, M. J.: Linear stratospheric gravity waves above convective thermal forcing, J. Atmos. Sci., 56, 2434–2446, 1999.

Rossow, W.B., Walker, A.W.,Beuschel D., and Roiter, M.: International Satellite Cloud Climatology Project (ISCCP) description of new cloud datasets. WMO/TD - No. 737, World Climate Research Programme (ICSU and WMO), Geneva, February 1996, pp. 115, 1996.

Röttger, J.: Structure and dynamics of the stratosphere and mesosphere revealed by VHF radar investigation, Pure Appl. Geophys., 118, 494–527, doi:10.1007/BF01586465., 1980.

Scherllin-Pirscher, B., Steiner, A. K., Kirchengast, G., Kuo, Y.-H., and Foelsche, U.: Empirical analysis and modeling of errors of atmospheric profiles from GPS radio occultation, Atmos. Meas. Tech., 4(9), 1875–1890, doi:10.5194/amt-4-1875-2011, 2011.

Scherllin-Pirscher, B., Steiner, A. K., Kirchengast, G., Schwärz, M., and Leroy, S. S.: The power of vertical geolocation of atmospheric profiles from GNSS radio occultation, J. Geophys. Res. Atmos., 2016JD025902, doi:10.1002/2016JD025902, 2017.

Schwärz, M., Kirchengast, G., Scherllin-Pirscher, B., Schwarz, J., Ladstädter, F., and Angerer, B.: Multi-mission validation by satellite radio occultation extension project—Final report, Tech. Rep. for ESA/ESRIN No. 01/2016, Wegener Center, University of Graz, Graz, Austria. [online] Available from: https://wegcwww.uni-graz.at/publ/wegcpubl/arsclisys/2016/Schwaerz-etal_MMValRO FinRep_Dec2016.pdf, 2016.

Skamarock, W.C., Klemp, J.B., Dudhia, J., Gill, D.O., Barker, D.M., Duda, M., Huang, X.-Y., Wang, W., Powers, J.G.: A Description of the Advaced Research WRF Version 3, NCAR Technical Note NCAR/TN-475+STR, 2008.

Steiner, A. K. and Kirchengast, G.: Error analysis for GNSS radio occultation data based on ensembles of profiles from end-to-end simulations, J. Geophys. Res, 110(D15), D15307, doi:10.1029/2004JD005251, 2005.

Steiner, A. K., Hunt, D., Ho, S.-P., Kirchengast, G., Mannucci, A. J., Scherllin-Pirscher, B., Gleisner, H., von Engeln, A., Schmidt, T., Ao, C.,Leroy, S. S., Kursinski, E. R., Foelsche, U., Gorbunov, M., Heise, S., Kuo, Y.-H., Lauritsen, K. B., Marquardt, C., Rocken, C., Schreiner,W., Sokolovskiy, S., Syndergaard, S., and Wickert, J.: Quantification of structural uncertainty in climate data records from GPS radio occultation, Atmos. Chem. Phys., 13, 1469–1484, doi:10.5194/acp-13-1469-2013, 2013.

Steiner, A. K., Lackner, B. C., Ladstädter, F., Scherllin-Pirscher, B., Foelsche, U., and Kirchengast, G.: GPS radio occultation for climate monitoring and change detection, Radio Sci., 46, RS0D24, doi:10.1029/2010RS004614, 2011.

725   Stephan, C. and Alexander, M. J.: Summer season squall-line simulations: sensitivity of gravity waves to physics parametrization and implications for their parametrization in global climate models, J. Atmos. Sci., 71, 3376–3391, doi: 10.1175/JAS-D-13-0380.1., 2014.